

AI-enabled rolling triboelectric nanogenerator for bearing wear diagnosis aiming at digital twin application



Fangyang Dong^{a,1}, Meixian Zhu^{b,1}, Yulian Wang^a, Zhixiang Chen^b, Yingwei Dai^b, Ziyue Xi^a, Taili Du^{a,b,*}, Minyi Xu^{a,**}

^a Dalian Key Lab of Marine Micro/Nano Energy and Self-Powered Systems, Marine Engineering College, Dalian Maritime University, Dalian 116026, China

^b Collaborative Innovation Research Institute of Autonomous Ship, Dalian Maritime University, Dalian 116026, China

ARTICLE INFO

Keywords:

Bearings
Fault diagnosis
Deep learning
Waveform analysis
Triboelectric nanogenerators

ABSTRACT

In the era of artificial intelligence (AI) and digitization, developing self-monitoring and smart-diagnosis bearings has become a meaningful yet challenging problem. This study investigates an AI-enabled bearing-structural rolling triboelectric nanogenerator (B-TENG), which can achieve condition monitoring and fault diagnosis for bearing wear. The geometrical structure of B-TENG is designed to directly use rolling balls as the freestanding layer. Besides, the sensing principle of triboelectric signal waveforms and the mapping mechanism of wear faults are firstly revealed through a signal decomposition method. Furthermore, a deep learning algorithm can classify different wear types, degrees and positions on rolling balls, with higher accuracies of 95.20~98.40 % for the feature components. The detection of wear degree related to bearing health and failure evolution is realized for the first time. The proposed B-TENG has the potential for digital twin application via interaction with professional simulation software according to the real-time diagnosis classified by AI.

1. Introduction

In the past few years, digital twin has been put forward more frequently in the concept of Internet of Things (IoTs) [1]. Combining the data collection of IoTs, the information processing of big data and the modeling analysis of AI, digital twin can achieve the assessment of current state, the diagnosis of past problems and the prediction of future developments, and give real-time analysis results, simulate various possibilities and provide comprehensive decision supports [2]. As a critical supporting component in rotating machines [3], bearing plays an irreplaceable role in almost all key industries and daily applications, including wheeled vehicles, wind turbines, aero engines, etc. [4], its digital twin (Fig. 1a) ought to be firstly and fully considered in Artificial Intelligence of Things (AIoTs) systems and Industrial 4.0 [5]. The sensory data is the key driver of digital twin [1]. Traditional sensing techniques encounter a challenge in terms of sensor arrangement [6], as modern machinery tends to be highly integrated. Earlier, a few intelligent bearing prototypes have been presented to monitor and detect the

working condition [7–9]. However, their functions still require additional sensors and systems, such as vibration sensor [10], thermal sensor and acoustic emission sensor [11,12], which increase the structural complexity, limiting their large-scale application for the digitization.

With more than a decade of development and refinement by researchers [13], triboelectric nanogenerator (TENG) technology has been studied as a promising solution for collecting energy from the environment to power wireless sensor signal transmissions [14], or for directly transmitting sensing information to IoT applications [15]. Noticeably, TENG-based sensors are more compatible with bearings, because it is easy to find two mated friction surfaces with reciprocating motion inside the bearing without external intrusion [16]. More importantly, the self-generated sensing output in response to the change or deformation of TENG makes the mapping relationship between the signal and the physical quantity more direct for further designs [13]. Therefore, using TENG to realize self-powered or self-sensing triboelectric bearings has been reported frequently. Meng et al. [17] developed a bearing-structured self-powered rotation sensor for multitasking motion

* Corresponding author at: Dalian Key Lab of Marine Micro/Nano Energy and Self-Powered Systems, Marine Engineering College, Dalian Maritime University, Dalian 116026, China.

** Corresponding author.

E-mail addresses: dutaili@dlmu.edu.cn (T. Du), xuminyi@dlmu.edu.cn (M. Xu).

¹ Fangyang Dong and Meixian Zhu contributed equally to this work

measurement, including speed, acceleration, and traveling distance. Choi et al. [18] presented a triboelectric roller bearing, using the output signals, the angular velocity and position of the components can be continuously monitored. Han et al. [19] proposed a triboelectric rolling ball bearing that can provide a peak power of $\sim 20 \mu\text{W}$ and identify the rotation speeds from 268 rpm to 1658 rpm. Gao et al. [20] designed a hybrid ceramic rolling element triboelectric bearing with the ultra-high rotating speed test at 16000 rpm. Li et al. [21] and Choi et al. [18] were earlier concerned about the triboelectric signals influenced by the defective balls or the removed rollers in their works. Despite a certain self-sensing ability endowed by TENG to bearings, it is still a challenge to achieve smart fault diagnosis in digital twins [22]. To date, the bearing faults, simulating extremely abnormal conditions, have been identified through frequency-domain analyses. Jiang et al. [23] and Han et al. [24] set up typical failure modes such as inner and outer ring cracks, ball loss, and gear defect for the self-sensing triboelectric bearings. By utilizing machine learning (ML) algorithms, the classification accuracies can exceed 90 % and 92 %. Gao et al. [5] developed a triboelectric metal-polymer plain bearing for identifying lubrication states, with the test accuracy of a deep learning (DL) model reaching 99.11 %. These works not only promote the applications of triboelectric technology on bearings, but also prove the feasibility of self-sensing and self-diagnosis for triboelectric bearings aided by AI technology.

By waiting until the extreme failure occurs to carry out corrective maintenance, the damage and loss may be unavoidable [25]. In industrial practice, the most common failure of bearings is slight defects occurring on rolling elements, inner and outer rings [26]. For these bearing failures to easily occur in the early stage, their detection and diagnosis have always been a puzzle [16]. Especially for process

production, predictive maintenance or active maintenance relying on early anomaly detections is of self-evident importance to prolong product lifecycle and reduce unplanned downtime [27]. Recently, Han et al. [16] realized the identification of the minor structural defects on outer rings, inner rings and rolling elements through the current frequency affected by the faults, with an accuracy of 80.1 % \sim 92.9 % for fault type and fault degree. However, wear of rolling elements, as one of the main modes of bearing initial failures [28], without obvious change in frequency [26,29], lacks effective real-time detection methods, thereby hindering the integrity of fault datasets and the advance of digital applications. Nonetheless, wear often brings about the generation of damaged surface and the change of friction state [30]. Benefiting from triboelectrification, TENG is especially adept at sensing these mutations. In our previous work [29], a flexible triboelectric layer for commercial bearings is designed to sense the partial wear of steel balls, and successfully achieved the diagnosis of different wear types by training the waveforms of electric signals in Automated ML. A comparison of the fault diagnosis works on triboelectric bearing has been summarized in Table S1 (Supporting Information). Yet, the mapping mechanism of the signal features with the corresponding wear faults, which will determine the rationality of the proposed triboelectric method for wear detection, is not clear. Furthermore, although triboelectric bearings have been applied to various condition monitoring, the exploration of bearing health monitoring by smart fault diagnosis is limited, thus cannot satisfy the requirements of its digital twins.

Herein, a rolling freestanding mode TENG (B-TENG) using AI technology is proposed for bearing health monitoring to achieve self-sensing, smart-diagnosis, and showing the potential to digital twin. B-TENG directly utilizes the bearing structure to detect and diagnose the wear of

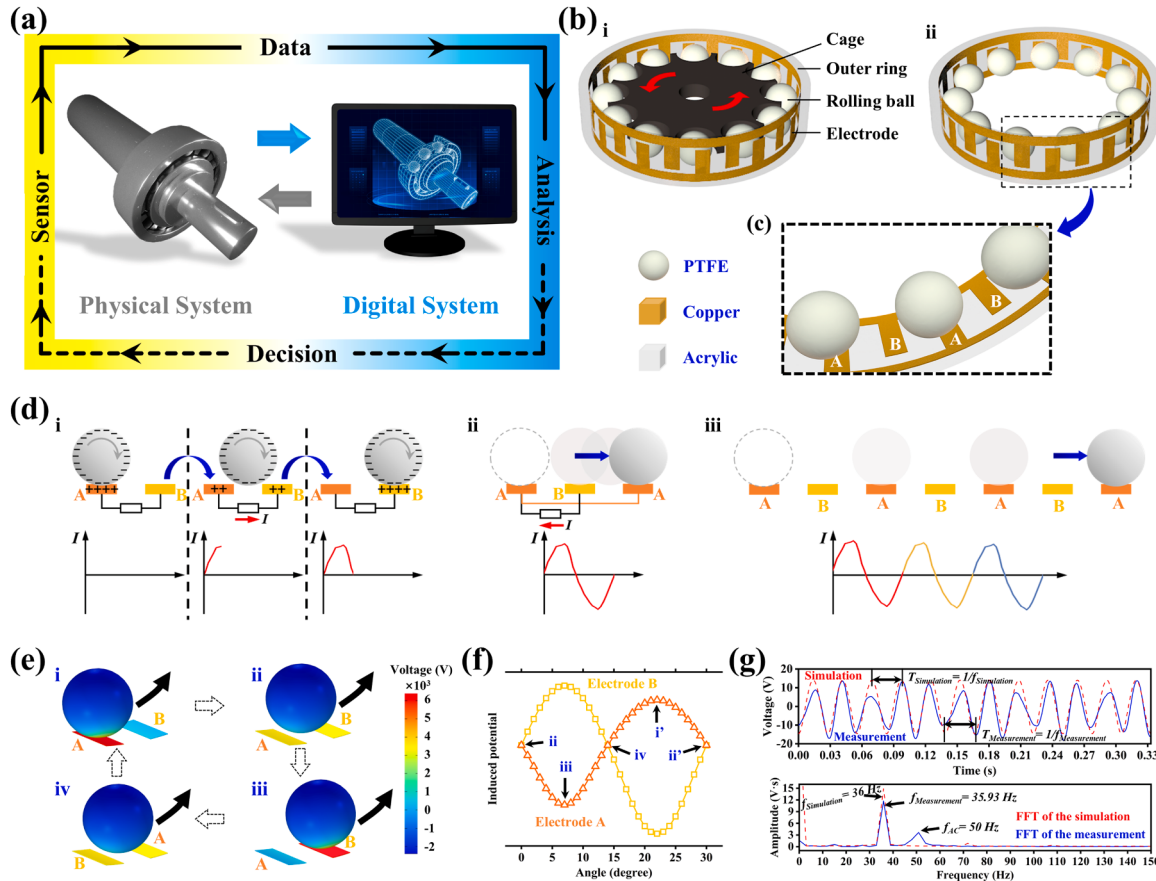


Fig. 1. Structure and working principle of B-TENG. (a) Digital application of the bearing. (b) Structural scheme of B-TENG. (c) Detailed view of the interdigitated electrodes. (d) Working mechanism of B-TENG. (e) COMSOL simulation results of the potential distribution at four charge transfer stages in one cycle. (f) Potential variations calculated by COMSOL on the two electrodes. (g) Comparisons of the simulated and measured voltage signals in time and frequency domains.

rolling balls, where the balls move freely as a self-driven sensor. The sensing principle and mapping mechanism between the wear faults and waveform features are firstly revealed via Seasonal and Trend decomposition using Loess (STL) and convolutional neural network (CNN) analyzing the triboelectric current waveforms. Then, a DL model based on CNN is developed to train and test the sample data of B-TENG with different wear types, degrees and positions on rolling balls. After extracting features of the wear faults by STL, the prediction accuracy of fault types reaches 98.40 %, which is extremely superior to the highest accuracy of 69.60 % with the original current signals. Moreover, for the first time, the detection of rolling ball wear degree related to the bearing health and even lifespan is realized in similar works. The identification accuracy of the minor defects with wear degrees of 1–5 % can reach 96 %, providing a considerable opportunity for the monitoring of bearing early failure and fault evolution. Next, the unilateral and bilateral wear of the bearing are also simulated. It shows a high accuracy of 95.20 % in identifying different positions distributed to the worn balls. Finally, a bearing health monitoring demonstration is established to diagnose the wear state of bearing balls in real-time and create the duplicate digital information of the above results in professional model simulation. In general, the proposed system together with AI algorithms illustrated a great potential aiming at digital twin application, e.g., condition assessment, failure diagnosis and tendency prediction of intelligent mechanical equipment.

2. Results and discussion

2.1. Configuration and working principle of B-TENG

Oriented to the research and application of smart fault diagnosis for bearings, B-TENG contains the basic elements of mechanical rolling bearings. As shown in Fig. 1b(i), the general structure of bearing is maintained by the outer ring, rolling balls and cage, adding two groups of interdigitated copper electrodes to form the rolling freestanding mode TENG with 12 polytetrafluoroethylene (PTFE) balls. Different from previous work, the direct contact combination of the copper electrodes and the PTFE balls is to obtain the most direct triboelectric signals that can reflect the running state of the rolling elements [21]. In the B-TENG sensor shown in Fig. 1b(ii), the PTFE balls are employed as the negative triboelectric layer, while two groups of interdigitated copper electrodes are attached to the inner surface of outer ring as the positive triboelectric layer and connected to the external circuit. The cage evenly separates the rolling balls and guides each freestanding ball to roll along the comb fingers of interdigitated electrode periodically (Fig. 1c), and thus providing alternating current (AC) to the external load. The number of copper electrode fingers is designed to be twice rolling PTFE balls and keep uniform distribution to ensure the maximum stable output of B-TENG [31]. This design ensures all balls leave and reach the same group of electrode fingers at the same time. The detailed methods for the fabrication of B-TENG sensor can be found in the “Experimental Section” and Fig. S1 (Supporting Information). Convenience to describe and comprehend, two groups of interdigitated electrodes are labeled as A and B respectively, as shown in Fig. 1c.

The working principle of B-TENG is illustrated in Fig. 1d. We idealize that PTFE balls are equidistant from each other by the isolation of the cage opening, and all of them are aligned with the copper electrode A at the original stage. After sufficiently contacting with the copper electrode A, the PTFE ball is prone to get negative charges distributed on the surface, leaving net positive charges on electrode A, since PTFE is more triboelectrically negative than copper [32]. When the PTFE ball is forced to roll towards electrode B, due to the electrostatic induction, the potential between electrode A and B begins to change, driving the electrons to electrode A through the external circuit and resulting in a positive peak waveform as shown in Fig. 1d(i). Similarly, the continued rolling of charged balls will propel the negative charges induced in electrode A flow back to electrode B, as displayed in Fig. 1d(ii), until the electric

potential is back to the original state, producing a negative peak in the current waveform. In Fig. 1d(iii), while the PTFE ball rolling over multiple pairs of electrode A and B, the alternating positive and negative peak values are produced in sequence on the time domain, which will form a continuous waveform. The whole process can be viewed as multiple combinations of the cycle shown in Fig. 1d(ii).

The above charge flows can also be explained by the variance of electric potential across two electrodes in open-circuit condition [17]. To verify the analyzed principle and visualize the output signal of B-TENG, the distribution of open-circuit voltage (V_{OC}) at four stages of a cycle is simulated by the finite element method from COMSOL Multiphysics software, as shown in Fig. 1e. In the open-circuit condition, as the charges cannot transfer between electrodes without the load, the V_{OC} is defined as the electric potential difference between two electrodes [33]. The detailed simulation settings of B-TENG are presented in the “Experimental Section”. Numerically calculated via COMSOL, Fig. 1f shows the continuous variation of the induced potentials with the rotation angle of PTFE balls. The stages corresponding to Fig. 1e are also plotted out, of which i' and ii' denote the next cycle. When the balls move, the distribution of potential on two electrodes changes in a complementary way. As a result, once passing a pair of electrodes generates a pair of AC peaks.

The quantifiable relationship of V_{OC} with time (i.e., with rotation angle at constant speed) can be obtained by subtracting the induced potentials on two electrodes:

$$V_{OC} = V_B - V_A \quad (1)$$

V_A and V_B are the induced potentials electrode A and B, respectively. Two groups of data points in Fig. 1f can be viewed as falling exactly on the ideal curves of $y = \sin x$ and $y = -\sin x$. Therefore, the relation of Eq. 1 can be listed as $V_{OC} \propto \sin t$, where t is time. The simulated voltage signal behaves as a “sinusoidal waveform” on the time domain, shown as the red dashed line in Fig. 1g. For the proposed B-TENG, the cage is interference fitted on the shaft to drive the rolling balls to rotate, so that the rotation frequency of the ball f_{ball} is consistent with the speed of the motor (i.e., the frequency of the motor f_{motor}). The relationship between them can be easily expressed as:

$$f_{ball} = f_{cage} = f_{motor} \quad (2)$$

In this design, the number of electrode finger pairs is equal to the balls, as $N_{electrode} = N_{ball} = 12$. According to the principle shown in Fig. 1d, the frequency of the voltage signal is then obtained as:

$$f_{voltage} = N_{electrode} \cdot f_{ball} \quad (3)$$

As shown in Fig. 1g, taking the rotation speed at 180 rpm ($f_{ball} = 3 \text{ Hz}$), the frequency of the simulated voltage signal is $f_{simulation} = 12 \times f_{ball} = 36 \text{ Hz}$, and the period is $T_{simulation} = 1/f_{simulation} = 27.78 \text{ s}$. Further, the measured voltage signal in the experiment is introduced to verify the validity of the simulation result, as shown by the blue solid line in Fig. 1g. After the fast Fourier transform (FFT), the frequency of the measured voltage can be directly calculated as $f_{measurement} = 35.93 \text{ Hz}$, and $T_{measurement} = 1/f_{measurement} = 27.83 \text{ ms}$. It can also be seen clearly from the waveform and the corresponding FFT spectrum in Fig. 1g, the frequency and period of the measured voltage fit well with the theoretical results. Here, the electric signal of B-TENG is self-generated without reliance on an external power source.

2.2. Output characteristics of B-TENG under different wear conditions

To test the electrical output performance of B-TENG, the measurement and acquisition system driven by a programmable AC motor is established as demonstrated in Fig. 2a. B-TENG and its companion bearing are installed on the shaft, being driven by the motor through a coupling. The signal acquisition flow is illustrated in Fig. 2b. The cage drives the rolling balls rotating in B-TENG while the outer ring keeps

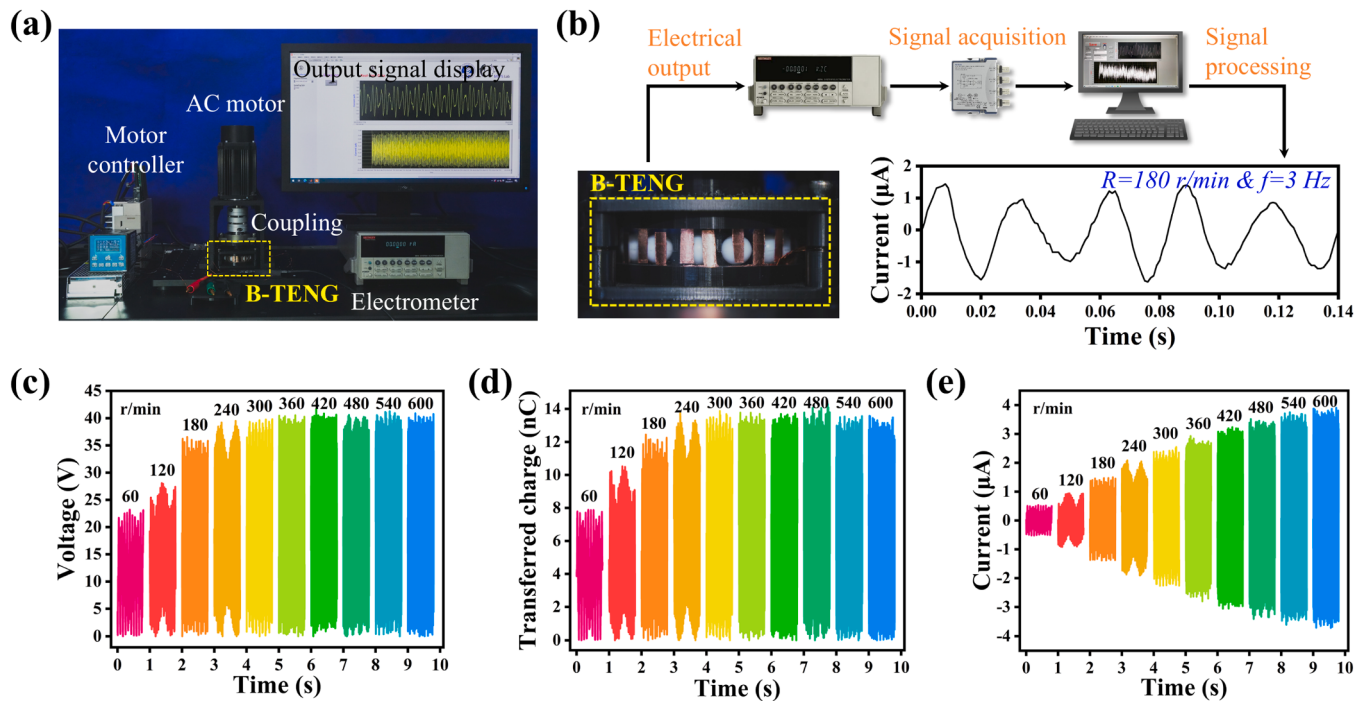


Fig. 2. Experiment process and electrical outputs of B-TENG. (a) Photograph of the measurement and acquisition platform of the bearing. (b) Flow chart of the data acquisition of B-TENG. (c) V_{OC} , (d) Q_{SC} and (e) I_{SC} under different rotation speeds.

stationary. And the movement of these balls across the electrode fingers will generate an electrical signal. The output signal is measured by the electrometer, and then transferred to the computer through a data acquisition (DAQ) unit and displayed on the screen. As illustrated in Fig. 2c, d and e, the electrical outputs of V_{OC} , transferred charge quantity (Q_{SC}) and short-circuit current (I_{SC}) are measured at different rotation speeds. The V_{OC} and Q_{SC} of B-TENG remain almost constant throughout the whole speed range except 60 and 120 rpm, and their peak-to-peak values are ~ 40 V and ~ 13.5 nC. This is because the V_{OC} is directly related to the constant transferred charges between the electrodes, depending on the contact area between rolling balls and electrodes [34]. The initial low speeds cannot guarantee the full contact. Similar phenomenon is mentioned in Ref. [19]. But in Fig. 2e, the I_{SC} almost linearly increases from 0.5 to 3.7 μ A with the rotation speed increasing from 60 to 600 rpm. It could be expressed as

$$I_{SC} = \frac{dQ_{SC}}{dt} = \frac{dQ_{SC}}{d\theta} \frac{d\theta}{dt} = 2\pi \frac{dQ_{SC}}{d\theta} f_{ball} \quad (4)$$

where $\frac{dQ_{SC}}{d\theta}$ is the charge change rate [24], which is an inherent parameter of B-TENG. In Eq. 2, f_{ball} is consistent with the frequency of the motor. Thus, the I_{SC} is also positively proportional to the rotation speed. As calculated in Fig. S2 (Supporting Information), the linear correlation (Pearson's r) between the mean value of current peaks and rotation speed is 0.98, which shows an ability in bearing speed sensing. The minimum stable speed of 180 rpm (3 Hz) is selected as the driving input for B-TENG, which ensures more signal details can be obtained. And referring to most bearing works [5,16,23,24], the I_{SC} is determined to be utilized in this study. The healthy current signal of B-TENG is displayed as the time-domain waveform in Fig. 2b, to clearly observe its characteristics, five consecutive cycles are intercepted. "Healthy" means the condition that the rolling balls being tested are perfect and without defects. As a freestanding layer TENG working on rolling mode, the shape of healthy I_{SC} is similar to the sinusoidal waves, consistent with the theoretical analysis and the previous works [35,36].

Structural defects of the rolling balls are artificially introduced by grinding, which is one of the common methods used in fault simulation experiments [11,16,29]. Under the same measurement conditions, one

ball wear, two balls wear, three balls wear and one ball loss, four different wear types are deliberately set, as shown in Fig. 3a, b, c and d. The damage quantity of each worn ball is 5 % of the complete weight. Photographs of wear details and weighing comparison are shown in Fig. S3 (Supporting Information). As can be seen intuitively in the time-domain signals of Fig. 2b and Fig. 3a to d, the waveform shapes of the health and four wear types are extremely similar. Quantitatively, the Pearson correlation between these current fragments is analyzed in Fig. 3e. Labels T1, T2, T3, T4 and T5 mark the five working conditions including health, one ball wear, two balls wear, three balls wear and one ball loss, respectively. This matrix summarizes the strength of the linear relationship between each two datasets of current signals [37]. The results show that all the five signals are positively correlated with each other (red area), even the minimum correlation coefficient of T2 (one ball wear) and T3 (two balls wear) is still 0.928. The differences between these similar signals may be reflected on the subtle changes in waveforms.

To extract the full sensory information, DL-assisted data analytics are applied [38]. CNN as a basic structure of DL provides an efficient way to automatically learn the representative features from the collected original signals, which has made great achievements in analyzing the triboelectric sensing signals [39,40]. Based on the characteristics of local connection and parameter sharing, CNN has been shown to be highly efficient in obtaining features from the shorter (fixed-length) segments of the overall dataset, where the relative locations of features can vary [38]. In addition, CNN is noted to be well-suited for processing the time series of sensor data [41]. In this study, a DL model is developed based on CNN to provide the high recognition performance of health and different wear signals through training the current waveforms. In terms of the training data, the triboelectric signals of five conditions (T1 to T5) are collected by repeating tests. Here, the original current data in time domain of five labels is directly used as the training samples, each sample is recorded with 1200 data points and 100 samples are collected for each label (75 % for training and 25 % for testing). The parameters used to build the CNN model refer to the settings in Shi's work [39] and exhibit in Fig. 3f and Table S2 (Supporting Information). The proposed network architecture of the bearing wear diagnosis consists of four

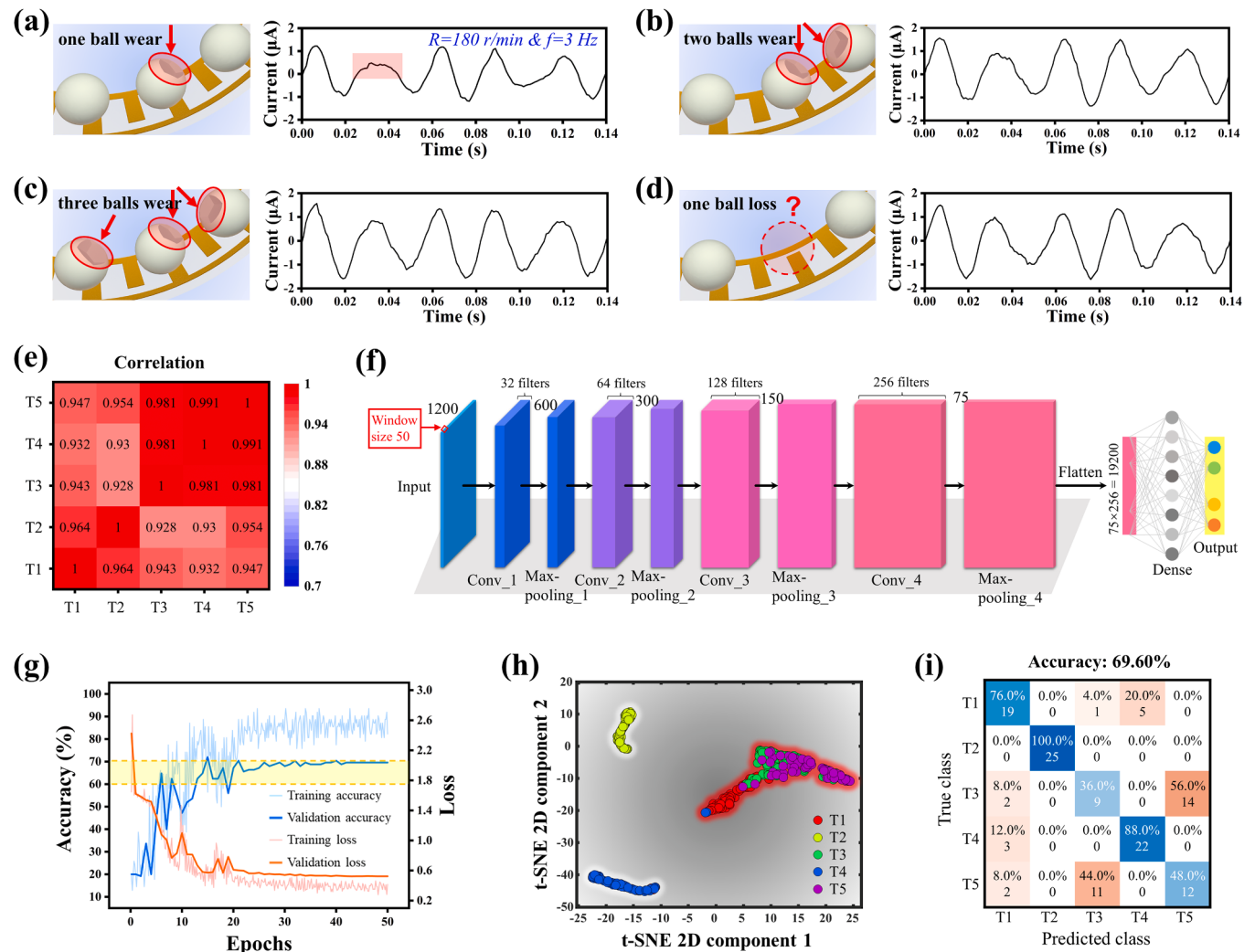


Fig. 3. Current signals of B-TENG with four wear types: (a) one ball wear, (b) two balls wear, (c) three balls wear, and (d) one ball loss. (e) Correlation heat map of the current data. (f) Detailed structure of the CNN training model. (g) Training process of the current data for five wear types. (h) Feature visualization of the penultimate layer using the t-SNE analysis. (i) Confusion matrix of the testing set from the current data (accuracy of 69.60 %).

convolutional layers, four max-pooling layers, and one fully connected layer, which output five types of the predicted results of health and wear. After the training process in CNN with 50 epochs, the maximum accuracy can be achieved, as shown in Fig. 3g. However, with the insignificant changes in different waveforms (Fig. 3e), it still raises a challenge to extract the diversity and representative features of the current signals under different working conditions only through the convolutional layer. Intuitively, the penultimate layer is visualized using the t-distributed Stochastic Neighbor Embedding (t-SNE) algorithm [42]. As shown in Fig. 3h, the abstract features from high dimensional space are reduced to two-dimensional (2D) space, and the same label is plotted in the same color. Some samples appear clustered, and others with different labels are confused together, especially T3 (two balls wear) and T5 (one ball loss). This is in line with the average recognition accuracy of five wear types only reaching 69.60 % (Fig. 3i). Among them, Label T3 presents the highest error rate with most testing samples being classified as Label T5. And nearly half of the Label T5's is misjudged as Label T3. The reason is their waveforms are too similar to each other, causing complete confusion. But the predicted rate of Label T2 is 100 %. This is because, the current signal of one ball wear marked as T2 already has the obvious local-changes, as shown in the red shadow of Fig. 3a, which is distinct from other labels. About others, the recognition rate is not outstanding. The superior accuracy of Label T2 evidences that

effective fault information is the key to ensuring the performance of smart fault diagnosis.

Moreover, to prove the local-change of Fig. 3c caused by the wear fault, the damage quantity of one ball wear is increased from 5 % to 25 % as shot in Fig. 4a. The corresponding fault current signals are shown in Fig. 4b. With a more obvious local-change in the red shadow than the low degree's, the waveform peak shows a “flat top” behavior. Similar phenomenon can be found in Ref. [33,35,43]. This is because the ball is difficult to maintain continuous rolling as the wear aggravates, gradually mixing with some sliding. Given the hard observation, the change of the motion pattern has been verified in ADAMS multi-body dynamics simulation software and displayed in Fig. 4c. The simulation settings and results in detail are presented in the “Experimental Section” and Movie S1 (Supporting Information). Until the degree of wear reaches 25 %, the diameter of the worn surface is 10 mm, which far exceeds the spacing between the electrode fingers. As shown in the principle schematic of Fig. 4d, at this time, the working mode of the worn ball has changed from the rolling freestanding with points to the sliding contact-separation with surfaces. The output charge from the worn surface can be quantified by Eq. 5 [31].

$$Q = (L/l)\sigma_{induced}A \quad (5)$$

where Q is the overall amount of charges that transport between

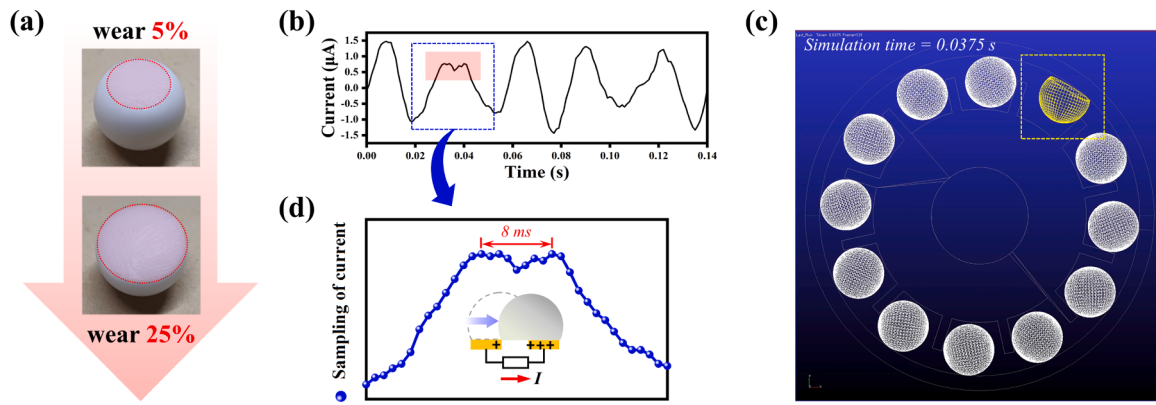


Fig. 4. Signal mutation of B-TENG caused by wear. (a) Photograph of the rolling balls with 5 % and 25 % wear degrees. (b) Current signal of one ball with 25 % wear. (c) Sliding motion of the worn ball in ADAMS. (d) Detailed sampling points of the current “flat top”.

electrodes, L is the sliding distance of the worn surface, l equals half the electrode spacing $l_{spacing}$, $\sigma_{induced}$ is the maximum density of the induced charges on electrodes, and A is the contact area.

Supplementary material related to this article can be found online at doi:10.1016/j.nanoen.2024.110550.

Hence, the corresponding current can be calculated as

$$I = \frac{dQ}{dt} = \frac{dQ}{dl}v \quad (6)$$

When the worn surface slides uniformly from electrode to electrode driven by the constant-speed, it can be seen from Eq. 6 that the current value remains stable, which will behave as “flat” in the current waveform, until completely detaching from the previous electrode. t is the time to charge transfer, that is, the time required to finish the misalignment between the worn surface and the electrode. It is noticed that the duration of the current peak is determined by the slider length (the worn surface in this study) and the rotation speed. Their relationship is emphasized in Ref. [35]. Quantitatively, the duration of the current “flat top” of 8 ms shown in Fig. 4d, should be equal to $t_{spacing}$, the time of the worn surface sliding through the electrode spacing of 5 mm (approximate a straight line).

$$t_{spacing} = \frac{L - l_{spacing}}{v} \quad (7)$$

$$v = n\pi D \quad (8)$$

By substituting the known parameters into Eqs. 7 and 8, $t_{spacing}$ is theoretically estimated to be ~ 8.04 ms. Therefore, the influence mechanism of the fault on the TENG signal is determined as the abnormal contact between the rolling ball and the metal electrodes lead by wear, which can be fed back to the change of the current waveform. The influence is also reflected in the output voltage, as Fig. S4 (Supporting Information) shows that, the V_{OC} (peak to peak) slightly increases with the worn area. The additional surface friction boosts the triboelectrification that is a surface charging effect dependent on area [35]. Above these analyses, the sensibility of TENG to the contact surface has been proved, which is well suited to detect the wear fault.

2.3. Data processing and fault diagnosis via STL decomposition and DL model

According to the prediction results shown in Fig. 3i, few fault features can be directly captured from the original current signal, thus different information of each label sample cannot be fully utilized, seriously affecting the performance of fault diagnosis. To obtain high-quality wear fault samples and significantly improve their diagnosis accuracy, the STL decomposition is introduced to extract critical fault information from the limited original data. As a typical feature

extraction technique, the signal decomposition algorithm decomposes the original data into different components, and then generates new waveform samples with obvious fault features. Specifically, the STL decomposition uses the locally weighted scatterplot smoothing (Loess) to smooth the time series data and decompose it into additive components, including season, trend and random [44], as shown in Fig. 5a. The main steps of the algorithm are seasonal smoothing and trend smoothing, after which, the trend values T_t and the season series S_t are got from the original values Y_t . And the random series R_t can be calculated according to Eq. 9:

$$R_t = Y_t - T_t - S_t \quad (9)$$

The mathematical details can be found in Note S1 (Supporting Information). For the current data of this study, as shown in Fig. 5b, the season component represents the AC variation, that is, the rolling balls across the electrode fingers periodically. The trend reflects that the current tends to be stable. On short datasets under a constant speed, the above two components are similar, and cannot provide representative information for different working conditions. And this is the main reason why these signals (Fig. 3e) are easily confused. The occasional anomalous observations do not affect the estimation of season and trend, but ultimately, they will be counted in the random component [29]. In theory, the random component contains the complete fault information. Compared with the original data, due to the redundant similar components being subtracted, the fault features are more prominent, which is conducive to the feature selection for the CNN model [45]. Therefore, the random component waveforms of the original current signals are used as new fault samples of rolling ball wear.

The random component waveforms of the five current signals in Fig. 3 are displayed in Fig. 5c, which reveals the featured patterns of the wear faults, including some important local-features. In these component waveforms with five signal cycles, two “one-cycle waveforms” at the corresponding positions are selected as the “local-feature 1” and “2” for analysis, as shown by the blue and red shadows. The original waveforms (blue and red dot plots) from the healthy signal are employed as the shape comparisons for observing the difference between the local-features. Since the rotation speed is constant, the horizontal direction (time axis) of the waveform image has been normalized. And the differences that can be exploited may come from amplitude, number of peaks and troughs, and holding time. The local-feature 1 of the healthy condition T1 almost coincides with the original waveform, indicating that there is no obvious anomaly in the data. But in T2 (one ball wear), its local-feature 1 shows a clear abnormal point on the normal peak, resulting in a “depression” on the waveform. Referring to the change in the original signal mentioned earlier, the reason is a sliding contact between the rolling ball and the electrode. With the increase of worn balls, continuous abnormal points are presented, such as the local-

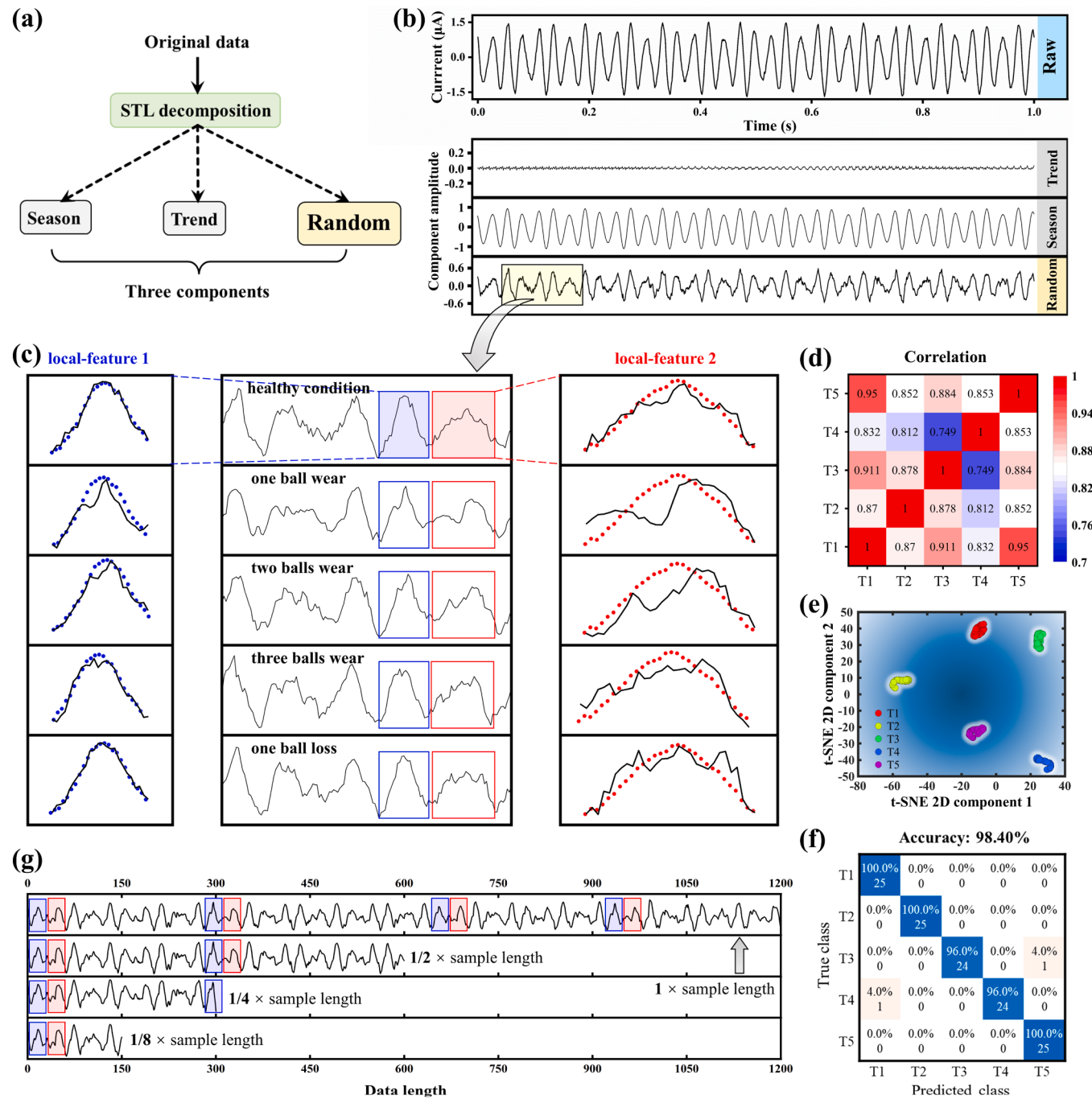


Fig. 5. Mapping mechanism and fault diagnosis based on the decomposed signals. (a) Schematic diagram of the STL decomposition process. (b) Three components of the original current signal decomposed through STL. (c) Random component waveforms of five current signals with different wear types. (d) Correlation heat map of the random components. (e) Feature visualization of the penultimate. (f) Confusion matrix of the testing set from the random components (accuracy of 98.40%). (g) Random component waveforms of ‘one ball wear’ with different data lengths.

feature 2 of T3 (two balls wear) and T4 (three balls wear). The number of anomalous points depend on the number of worn balls. This is because B-TENG triggers multiple ball defects, causing a continuous change in the time series of the local-feature, which will bring a clear distinction for CNN [38]. The correlation between the random component waveforms decreased significantly, as shown in Fig. 5d. Unexpectedly, the local-feature of T5 (one ball loss) presents a high coincidence degree with the original waveform, and their correlation coefficient reaches 0.95. This may be because the remaining balls are intact, without any worn surface, and still keep the continuous rolling.

Under the same setting of the CNN model, the newly generated

random components are used as five label samples (T1 to T5) for fault type recognition, which also corresponds to five conditions of health, one ball wear, two balls wear, three balls wear and one ball loss, respectively. Because comes from the original data, there are still 100 samples for each label with a sample length of 1200 data points. It is noted that the local-feature waveforms shown in Fig. 5c include about 20 and 30 points, respectively. The length of the sliding window following the initial setting is determined as 50 to ensure that at least one local-feature information can be fully covered. Fig. S5 (Supporting Information) displays the training process of the CNN model, where the accuracy rates of both training and validation sets increase rapidly with

the training epochs. After the 20 epochs, the oscillation amplitude of accuracy curves has reduced to less than 10 %, and the accuracy and loss curves tend to be horizontal after 40 epochs, indicating that the model has converged and generalized enough to avoid overfitting. When the training time continues, the performance of the model is no longer significantly improved. To balance the model quality and computational complexity, the training epochs are set as 50 for the five label samples. Moreover, the penultimate layer is also visualized using t-SNE for proving the effectiveness of the model prediction. As shown in Fig. 5e, the decomposed random component samples present a good clustering effect, because the points in the same color are tightly hugged together and keep a long distance from other colors, indicating that the model can fully mine the abstract features of different labels. Compared with Fig. 3h, the STL decomposition brings more obvious fault features under the same input.

Fig. 5f shows the confusion matrix of the five labels classification using the random components. The results of other components are also provided in Fig. S6 (Supporting Information). It is obvious that the trained model has a higher prediction accuracy of 98.40 % compared to that using the original data (69.60 %), season components (66.40 %) or trend components (52.80 %), indicating that the effective data features play an important role in improving the recognition performance of the system. Of the total 125 ($100 \times 0.25 \times 5$) predicted results, only two fault waveforms are misjudged as other labels. In Label T4 (three balls wear), maybe the position of the abnormal points is close to the waveform crest, which is misjudged as the healthy condition T1 by the model. To the surprise, the predicted rate of Label T5 is 100 %. Although overlap the healthy waveform, all the waveforms of one-ball-loss condition are successfully detected. It can be inferred that the loss of the rolling ball is a serious fault, which will bring different changes from other wear faults. After introducing the STL decomposition to extract the features of the current signal, the diagnosis accuracy of wear faults is considerably improved. Then, the accuracies of other commonly adopted DL models are compared in Fig. S7 (Supporting Information), including deep neural network (DNN) and long short-term memory (LSTM) network. Their structure and parameters can be found in Table S3 and S4 (Supporting Information). The results show that the proposed CNN has the highest diagnosis accuracy under the approximate settings. The great feasibility of intelligent bearing fault diagnosis method via STL and CNN can be established.

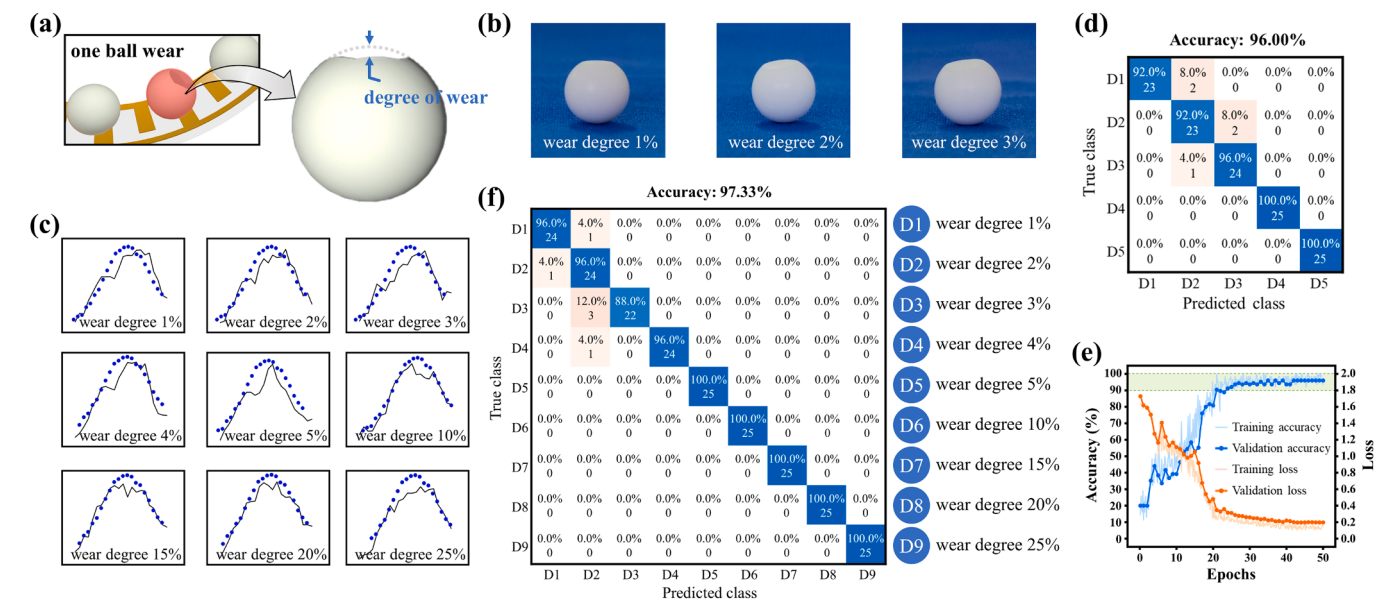
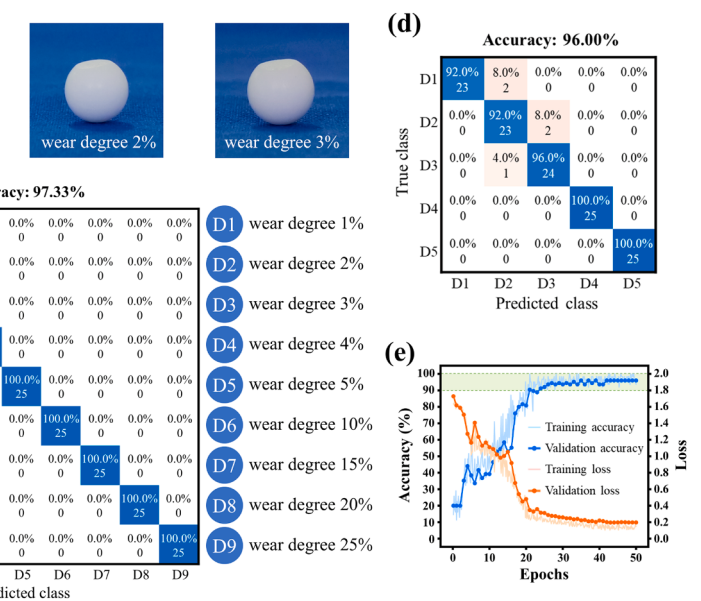


Fig. 6. Wear degree detection via STL and CNN. (a) Schematic and (b) photograph of rolling balls with the wear degrees of 1 %, 2 % and 3 %. (c) Local-features of different wear degrees. (d) Confusion matrix and (e) training process of the minor wear prediction (accuracy of 96.00 %). (f) Confusion matrix of the nine-label classification with all one-ball-wear conditions (accuracy of 97.33 %).

More importantly, STL is robust to the input data length. As demonstrated in Fig. 5g, whether 1/8, 1/4, 1/2 or 1 sample length, their random component waveforms in the same time domain remain unchanged. Moreover, it can be noticed that the fault local-features are repeated over the samples, rather than occurring by accident. In theory, the fault information can be extracted without relying on a large and complete input, once the collected data contains. This is of great significance for the practical engineering scenarios, where the monitored data is often discontinuous by the limitations of energy and transmission.

2.4. Wear degree and position detection with B-TENG

As one of the most common incipient failure modes of bearings, the timely response at the beginning of the wear of moving parts can avoid major accidents. Therefore, the accurate detection of the wear degree of rolling balls is of great concern, especially the slight wear that occurred in the initial stage of machine service. Focusing on one ball wear, the current signals with different wear degrees are selected for further discussion, including minor wear (wear degree of 1 %, 2 %, 3 %, 4 % and 5 %) and obvious wear (wear degree of 5 %, 10 %, 15 %, 20 % and 25 %). The percentage of wear degree is defined as the weight loss after wear divided by the weight of the perfect ball. The schematic of wear degree is shown in Fig. 6a, and all the wear details and weighing comparison are shown in Fig. S3 (Supporting Information). The actual photos of rolling balls with the wear degrees of 1 %, 2 % and 3 % are shot in Fig. 6b, whereas other vibration sensors commonly used in bearings are helpless for such slight wear [12,26,46]. Here, the typical local-features of the current random components from different wear degrees are displayed in Fig. 6c. Even 1 % wear can be sensed by B-TENG and visualized by the STL decomposition. Accurate diagnosis of wear degree deterioration will lay the groundwork for bearing health monitoring. Fig. 6d and Fig. S8 (Supporting Information) present the prediction results of the minor wear and obvious wear, respectively. The average accuracy for 1–5 % wear is 96 %, in which the error samples are only distributed in the wear degrees less than 3 %. And visualizing it training process in Fig. 6e, the same model still converges rapidly within 40 epochs, which highlights the advantage of STL + CNN in extracting and learning the abstract features. Not surprisingly, the prediction rate of the obvious wear (5–25 %) can reach 98.40 %. Furthermore, the



nine-label classification of all one-ball-wear conditions (1 %, 2 %, 3 %, 4 %, 5 %, 10 %, 15 %, 20 % and 25 %) is tested to verify the model portability for bearing health monitoring in the wear continuously deteriorating. By setting the batchsize from 6 to 15, the iterations in each epoch are increased to cope with the growth of the data dimensions. Fig. 6f shows the confusion matrix of the nine-label classification. After training, the model can successfully distinguish nine kinds of increasing wear degrees with an accuracy of 97.33 %. The proposed method shows a prospect to monitor the fault evolution and even the whole lifecycle of bearings. In addition, it is noted that the local-features 1 with 10 % and 15 % wear are similar to that of two balls wear (5 % + 5 %) and three balls wear (5 % + 5 % + 5 %). This proves that the current waveform is a superposition of the electrical output from each ball. However, as mentioned earlier, the local-feature 2 is highly related to the number of worn balls, so they do not confuse each other. The proof is given by the confusion matrices of one ball wear (10 %) with two balls wear and one ball wear (15 %) with three balls wear, as shown in Fig. S9 (Supporting Information).

Bearing offload from the improper assembly will cause unilateral or bilateral wear [28]. The sensing of B-TENG to different wear positions is verified by setting different distributions of the two worn balls (5 %). As shown in Fig. 7a, among the twelve rolling balls arranged along the inner wall of the outer ring, the condition of two worn balls in adjacent position is labeled P1, the condition of two worn balls spaced by one normal ball is labeled P2, ..., until the condition of two wear balls spaced by five normal balls (opposite position) is labeled P6. The actual photos of P1 and P6 are shot in Fig. 7b. Through Fig. 7c, the typical local-features from different wear positions show that their basic waveform shape is associated with that of two balls wear. With spacing, the synchronicity of two worn balls becomes worse, and the feature waveforms begin to differ. Then, the six-label recognition experiment is carried out for the conditions of P1 to P6, and the prediction results are displayed in Fig. 7d. Label P2 and P3 are seriously confused, since the closer positions lead to the convergence of two conditions. Nevertheless, other results show a sensitivity to the fault position. By taking each 50 % sample of Label P2 and P3 to form a new label (P2 + P3), the five-label recognition results are obtained in Fig. 7e. The average predicted accuracy of different wear positions is up to 95.20 %. In particular, the detection rates of the adjacent (P1) and opposite (P6) positions are 100 % and 92 %, respectively. This is of great significance for bearings to determine the wear mode and analyze the load direction. For comparison, the classified and predicted results using original current data

of different wear degrees and different wear locations can be found in Fig. S10 (Supporting Information). It is further proved that the feature preprocessing by the STL decomposition helps to improve the performance of the CNN model in this study.

2.5. Digital twin demonstration with bearing health monitoring system

Bearings, owing to their extensive applications, have played a pivotal role in almost all key industries and will serve as an indispensable foundational component in the future digital twin systems. To demonstrate the application potential of the triboelectric wear sensing represented by B-TENG, a digital twin-oriented bearing health monitoring system is constructed, enabling the non-destructive detection and the real-time diagnosis of bearing wear, where the recognition results in the real space can be real-timely projected into a virtual space. The process flow of establishing and using the system is explained in Fig. 8a. When the system is running, the triboelectric current signal of the B-TENG sensor can be collected regularly, whereafter the trained CNN model can in-time predict the signal passed the feature extraction. After extracted with the STL decomposition and classified with the CNN model, the real-time signal diagnosis system is realized as shown in Fig. 8b and Movie S2 (Supporting Information). The screen displays the real-time collected signal, the post-decomposition signal waveform, and the corresponding predicted result and picture for the presupposed fault. The system has successfully achieved the real-time accurate diagnosis of healthy condition and four faults (one ball wear, two balls wear, three balls wear, and one ball loss). Then, connecting the real-time diagnosis system with the dynamics simulation software, the digital twin application is conceptualized as shown in Fig. 8c. Once the real-time diagnosis result is received, the bearing digital-twin body corresponding to the wear fault is called and begins to run in ADAMS software, as demonstrated in Movie S3 (Supporting Information). The diagnosis results will dynamically adjust the input parameters of digital models (such as the number of worn balls), so that the real failure can be correctly reflected and analyzed in ADAMS. To achieve digital twin in future, more discretized bearing digital models under different working conditions need to be prepared. Its real-time requirement is guaranteed by real-timely receiving the diagnosis results classified by AI and real-timely calling the corresponding simulations. When digital-twin body is called and analyzed, the simulation time can be asynchronous but delicate to ensure the accuracy. Digital twin supported by professional software will facilitate the provision of comprehensive and precise measurements

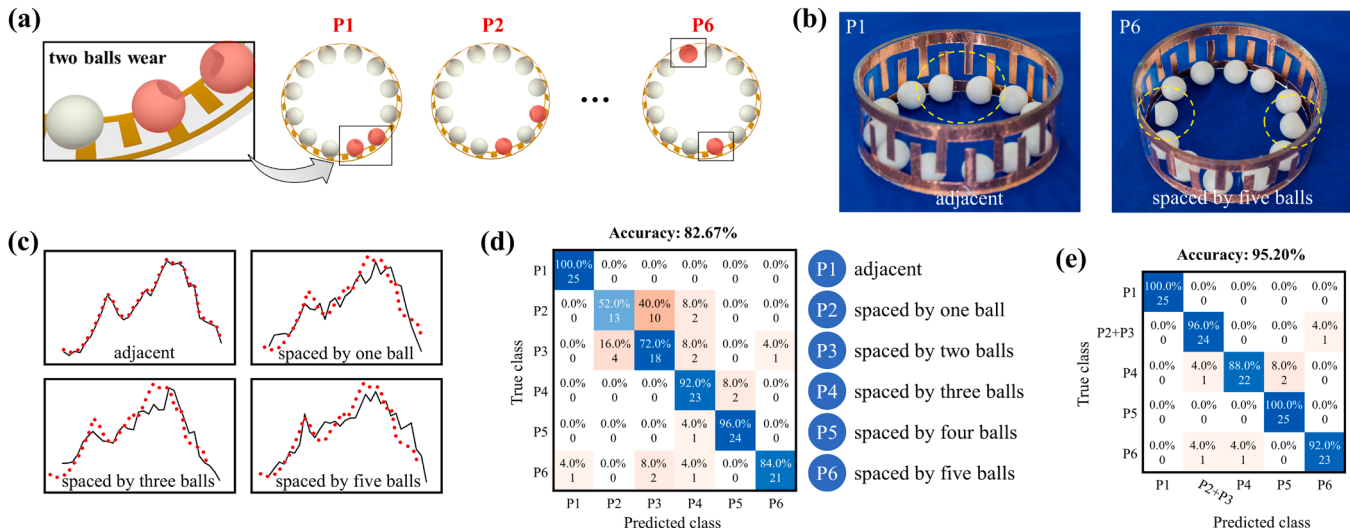


Fig. 7. Wear position detection via STL and CNN. (a) Schematic of different wear positions. (b) Photograph of two worn balls in adjacent and opposite positions. (c) Local-features of different wear positions. (d) Confusion matrix and (e) label-adjusted confusion matrix of wear position prediction (accuracies of 82.67 % and 95.20 %).

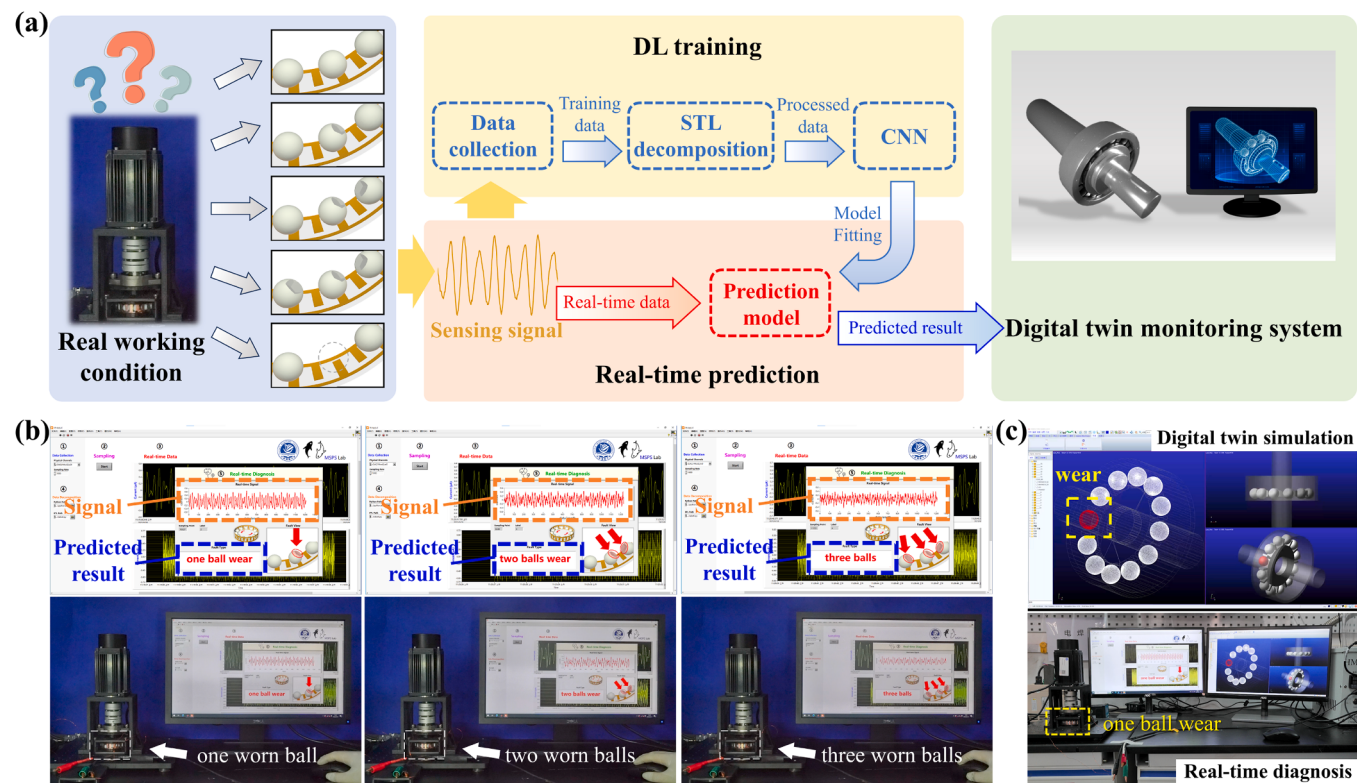


Fig. 8. Digital twin-oriented bearing health monitoring system. (a) Process flow of establishing and using the system. (b) Real-time diagnosis for different bearing wear conditions. (c) Bearing digital-twin body in ADAMS software.

for intelligent decision and regulation.

Supplementary material related to this article can be found online at doi:10.1016/j.nanoen.2024.110550.

Given the differences between laboratory settings and real-world scenarios, B-TENG and the system may face limitations in industrial applicability and model generalization. Potential challenges may arise from bearing compactness and balance, applications on steel-based bearings, failure diversity and variability, wireless and self-powered systems, etc. Our subsequent works will focus more on maintaining traditional bearing structures and exploring transfer learning for the trained models. Going forward, further investigation is required into such as implantable structures, integrated circuits, embedded systems, incremental learning, adaptive models and model interpretability.

3. Conclusion

In summary, an AI-enabled rolling TENG is developed for self-sensing and smart-diagnosis of intelligent bearings by utilizing the triboelectric principle. Considering the scalable measurement, B-TENG is directly derived from an actual bearing structure, where the rolling PTFE balls driven by the cage serve as a movable freestanding layer to participate in the triboelectrification with the interdigitated copper electrodes. In the investigation of bearing ball wear fault diagnosis, the STL decomposition algorithm is introduced to extract fault features in the indistinguishable current signals. And the time-domain feature waveforms are analyzed to reveal the sensing principle of B-TENG. Then, a CNN model is proposed. Through training, the considerably accurate recognition of different wear types, degrees and positions on rolling balls can be achieved with 95.20~98.40 %. Especially, the minor defects of rolling ball with wear rates of 1~5 % are paid attention, which shows the effective detection capacity for the bearing early failure and fault evolution. Finally, a bearing health monitoring system aimed at digital twin application is demonstrated, which can real-timely diagnose the wear state of bearing balls, thereby calling a bearing digital-twin

body in the professional model simulation software. In general, the marriage of triboelectric effects and AI algorithms is verified to monitor the health condition of target bearings, presenting a strong potential in the field of fault diagnosis for intelligent machinery. The proposed digital-twin system can real-timely sense, accurately diagnose and actively reflect the state of physical objects through the TENG-based measurement, DL-assisted analysis and model-mapped simulation, making a pioneering exploration to applying triboelectric sensing technology in digital twins.

4. Experimental section

4.1. Fabrication of B-TENG

B-TENG consists of an Acrylic outer ring, two groups of interdigitated copper electrodes, twelve PTFE balls and a Polylactic acid (PLA) cage. The dimensions of B-TENG refer to a SKF63009-2RS1 deep groove ball bearing. The outer ring with a width of 25 mm, inner diameter of 66 mm and wall thickness of 2 mm, was cut by a laser cutting machine from a transparent acrylic tube for observation. The interdigitated copper electrodes consist of two groups of complimentary finger arrays, each of which has twelve electrode fingers, cut from two pieces of copper film with a thickness of 0.06 mm. The electrode width is also designed to be 25 mm to ensure the rolling balls only contact with the electrode fingers. The finger width is 3.7 mm and the spacing between two adjacent fingers is 5 mm. After cleaning and drying the outer ring, the interdigitated electrodes were attached to the inner surface. The diameter of the PTFE ball is 10.5 mm. The cage was printed by a 3D printer (Z6, Dwmaker) with PLA material, and its diameter is 58 mm, which spaced these balls evenly and guided their movement.

4.2. Setting of the wear faults

Different wear of rolling balls is simulated and fabricated by

grinding. While a perfect PTFE ball was being held in a manual fixture (#15, GuanGO), its exposed surface was polished with a file. The weight loss was weighed continually by an electronic balance (FA2004N, SHANGPING) to determine the wear degree. Such as 5 % wear, the worn-off weight can be calculated by $1.31 \times 0.05 = 0.0655$ g, since the weight of a perfect ball is 1.31 g. The above process was repeated for different wear degrees.

4.3. Electrostatic and dynamic simulation

3D models were built according to the actual dimensions of B-TENG. For electrostatic simulation via COMSOL software (COMSOL Multiphysics 5.6, COMSOL), the outer surface of the PTFE ball was assigned a surface charge density of -8×10^{-6} C m⁻² [17]. In open-circuit condition, the two planar electrodes were both assigned the corresponding suspension potential and grounding. For dynamic simulation via ADAMS software (Adams 2020, MSC), the component models (cage, rolling balls, outer ring and sealing covers) of B-TENG were first established and assembled by SOLIDWORKS software (SOLIDWORKS 2019, Dassault Systèmes). Then, the model file was imported into ADAMS software. The drive function of the revolute pair was typed as $1080\ d * \text{time}$ while 180 rpm. The simulation step size in this study is set at 0.001 s.

4.4. Data collection and DL training

The experimental platform consisted of an AC servo motor (750 W, 3000 rpm, HECHUANG), a frequency converter (DKC-Y110, YIXING), a rotor shaft (aluminum alloy, diameter 20 mm × length 90 mm) and a bearing pedestal (SKP004, KIF). All the test components were bolted to the optical platform (aluminum, 300 mm × 300 mm × 13 mm). The generated triboelectric signals of B-TENG were acquired by a DAQ card (9215, NI) in an electrometer (6514, Keithley) with a sampling frequency of 1000 Hz. In setting the training data for DL training, a current signal was recorded with 1200 data points and 100 samples were collected for each wear condition, where 75 samples were used for training (75 %) and 25 samples for testing (25 %). Using the above settings but after the STL decomposition, the random components of all current samples were used as the new samples. The CNN models were configured as follows: the categorical cross-entropy function was applied as the loss function, the adaptive moment estimation was used as the update rule due to its optimization convergence rate, and prediction accuracy was used to evaluate the model training. Each time the specified 20 epochs passed, the learning rate was reduced by 10 times. These models were developed in MATLAB software (MATLAB R2022a, MathWorks) and trained on an ordinary performance computer (CPU: i5-10400F 3.60 GHz, Intel; GPU: GeForce GTX 1050Ti, NVIDIA).

4.5. Demonstration of the digital twin application

The triboelectric current signals from B-TENG were first connected to the analog-to-digital converter of the electrometer. The acquired signals were sent to a LabVIEW-based computer by USB cable communication instantly. LabVIEW software (LabVIEW 21.0, NI) called Python 3.6.8 with the STL file and the trained model to process the received signal and display the predicted result on its front panel. When the first predicted result was detected, the corresponding digital-twin body began to run in ADAMS software. And then, the regular diagnosis results will dynamically adjust the input parameters and other digital models, so that the real failures can be correctly reflected and analyzed in the simulation software.

CRediT authorship contribution statement

Minyi Xu: Writing – review & editing, Supervision, Project administration, Funding acquisition. **Ziyue Xi:** Visualization, Resources. **Taili**

Du: Writing – review & editing, Supervision, Project administration, Funding acquisition. **Meixian Zhu:** Visualization, Software, Methodology, Investigation, Formal analysis, Data curation, Conceptualization. **Yulian Wang:** Software, Data curation. **Zhixiang Chen:** Visualization, Resources, Data curation. **Yingwei Dai:** Software, Data curation. **Fangyang Dong:** Writing – original draft, Visualization, Software, Project administration, Methodology, Investigation, Formal analysis, Data curation, Conceptualization.

Declaration of Competing Interest

The authors declare that they have no known competing financial interests or personal relationships that could have appeared to influence the work reported in this paper.

Acknowledgements

The work is supported by the National Natural Science Foundation of China (Grant Nos. 52101345, 52101400), the Scientific Research Fund of the Educational Department of Liaoning Province (Grant No. LJ212410151013, LJKMZ20220359), the China Postdoctoral Science Foundation (Grant No. 2024M750297), and the Fundamental Research Funds for the Central Universities (Grant No. 3132024210).

Appendix A. Supporting information

Supplementary data associated with this article can be found in the online version at doi:[10.1016/j.nanoen.2024.110550](https://doi.org/10.1016/j.nanoen.2024.110550).

Data Availability

Data will be made available on request.

References

- [1] Q.L. Qi, F. Tao, T.L. Hu, N. Anwer, A. Liu, Y.L. Wei, L.H. Wang, A.Y.C. Nee, Enabling technologies and tools for digital twin, *J. Manuf. Syst.* 58 (2021) 3–21, <https://doi.org/10.1016/j.jmsy.2019.10.001>.
- [2] H. Boyes, T. Watson, Digital twins: an analysis framework and open issues, *Comput. Ind.* 143 (2022) 19, <https://doi.org/10.1016/j.compind.2022.103763>.
- [3] R.N. Liu, B.Y. Yang, E. Zio, X.F. Chen, Artificial intelligence for fault diagnosis of rotating machinery: a review, *Mech. Syst. Signal Proc.* 108 (2018) 33–47, <https://doi.org/10.1016/j.ymssp.2018.02.016>.
- [4] Y. Zhang, W. Wang, X. Wu, Y.G. Lei, J.Y. Cao, C. Bowen, S. Bader, B. Yang, A comprehensive review on self-powered smart bearings, *Renew. Sust. Energ. Rev.* 183 (2023) 23, <https://doi.org/10.1016/j.rser.2023.113446>.
- [5] M. Gao, T.D. Sun, Y.H. Li, Z.X. Zhang, C.K. Lee, J. Choi, AI-enabled metal-polymer plain bearing based on the triboelectric principle, *Adv. Funct. Mater.* 11 (2023), <https://doi.org/10.1002/adfm.202304070>.
- [6] W. Zhao, Y.M. Zhang, Reliability analysis of random vibration transmission path systems, *Mech. Syst. Signal Proc.* 113 (2018) 77–89, <https://doi.org/10.1016/j.ymssp.2017.06.037>.
- [7] T. Koike, T. Ishikawa, H. Isobe, Combined sensor and bearing assembly, US7583079, 2009-09-01.
- [8] T. Ozaki, T. Ishikawa, K. Nishikawa, Wheel support bearing assembly equipped with sensor, US8439568, 2013-05-14.
- [9] J. Erskine, K. Hamilton, B. Murray, A.C.v.d. Ham, Module for determining an operating characteristic of a bearing, US9453780, 2016-09-27.
- [10] W. Zhou, T.G. Habetsler, R.G. Harley, Bearing condition monitoring methods for electric machines: A general review, in: IEEE International Symposium on Diagnostics for Electric Machines, Power Electronics and Drives, Ieee, Cracow, POLAND, 2007, pp. 11–14. (<http://doi.org/10.1109/DEMPED.2007.4393062>).
- [11] A. Mohammed, S. Djurovic, Electric machine bearing health monitoring and ball fault detection by simultaneous thermo-mechanical fibre optic sensing, *IEEE Trans. Energy Convers.* 36 (2021) 71–80, <https://doi.org/10.1109/tec.2020.3003793>.
- [12] B. Van Hecke, J. Yoon, D. He, Low speed bearing fault diagnosis using acoustic emission sensors, *Appl. Acoust.* 105 (2016) 35–44, <https://doi.org/10.1016/j.apacoust.2015.10.028>.
- [13] F.R. Fan, Z.Q. Tian, Z.L. Wang, Flexible triboelectric generator!, *Nano Energy* 1 (2012) 328–334, <https://doi.org/10.1016/j.nanoen.2012.01.004>.
- [14] S.B. Lv, H.Y. Li, Y.Y. Xie, B.B. Zhang, B.C. Liu, J. Yang, H.Y. Guo, Z.B. Yang, Z. M. Lin, High-performance and durable rotational triboelectric nanogenerator leveraging soft-contact coplanar charge pumping strategy, *Adv. Energy Mater.* 13 (2023) 9, <https://doi.org/10.1002/aenm.202301832>.

- [15] H.Y. Li, S.B. Lv, B.B. Zhang, B.C. Liu, J. Yang, H.Y. Guo, Y.Y. Xie, Z.M. Lin, High power and low crest factor of direct-current triboelectric nanogenerator for self-powered optical computing system, *Energy Environ. Sci.* 16 (2023) 4641–4649, <https://doi.org/10.1039/d3ee01930f>.
- [16] T.Y. Han, X.J. Ding, H. Hu, Z.K. Peng, X. Shi, S.T. Hu, Health monitoring of triboelectric self-sensing bearings through deep learning, *Measurement* 220 (2023) 11, <https://doi.org/10.1016/j.measurement.2023.113330>.
- [17] X.S. Meng, H.Y. Li, G. Zhu, Z.L. Wang, Fully enclosed bearing-structured self-powered rotation sensor based on electrification at rolling interfaces for multi-tasking motion measurement, *Nano Energy* 12 (2015) 606–611, <https://doi.org/10.1016/j.nanoen.2015.01.015>.
- [18] D. Choi, T. Sung, J.Y. Kwon, A self-powered smart roller-bearing based on a triboelectric nanogenerator for measurement of rotation movement, *Adv. Mater. Technol.* 3 (2018) 8, <https://doi.org/10.1002/admt.201800219>.
- [19] Q.K. Han, Z. Ding, Z.Y. Qin, T.Y. Wang, X.P. Xu, F.L. Chu, A triboelectric rolling ball bearing with self-powering and self-sensing capabilities, *Nano Energy* 67 (2020) 10, <https://doi.org/10.1016/j.nanoen.2019.104277>.
- [20] S. Gao, Q.K. Han, X.N. Zhang, P. Pennacchi, F.L. Chu, Ultra-high-speed hybrid ceramic triboelectric bearing with real-time dynamic instability monitoring, *Nano Energy* 103 (2022) 13, <https://doi.org/10.1016/j.nanoen.2022.107759>.
- [21] X.H. Li, C.B. Han, T. Jiang, C. Zhang, Z.L. Wang, A ball-bearing structured triboelectric nanogenerator for nondestructive damage and rotating speed measurement, *Nanotechnology* 27 (2016) 9, <https://doi.org/10.1088/0957-4484/27/8/085401>.
- [22] M. Cerrada, R.V. Sánchez, C. Li, F. Pacheco, D. Cabrera, J.V. de Oliveira, R. E. Vásquez, A review on data-driven fault severity assessment in rolling bearings, *Mech. Syst. Signal Proc.* 99 (2018) 169–196, <https://doi.org/10.1016/j.ymssp.2017.06.012>.
- [23] Z.Y. Jiang, S. Gao, Y. Kong, P. Pennacchi, F.L. Chu, Q.K. Han, Ultra-compact triboelectric bearing based on a ribbon cage with applications for fault diagnosis of rotating machinery, *Nano Energy* 99 (2022) 10, <https://doi.org/10.1016/j.nanoen.2022.107263>.
- [24] Q.K. Han, Z.Y. Jiang, X.P. Xu, Z. Ding, F.L. Chu, Self-powered fault diagnosis of rolling bearings based on triboelectric effect, *Mech. Syst. Signal Proc.* 166 (2022) 14, <https://doi.org/10.1016/j.ymssp.2021.108382>.
- [25] M.G. Deighton, *Maintenance Management*, in: M.G. Deighton (Ed.), *Facility Integrity Management*, Gulf Professional Publishing, Boston, 2016, pp. 87–139.
- [26] I. El-Thalji, E. Jantunen, A summary of fault modelling and predictive health monitoring of rolling element bearings, *Mech. Syst. Signal Proc.* 60–61 (2015) 252–272, <https://doi.org/10.1016/j.ymssp.2015.02.008>.
- [27] A. Aboshosha, A. Haggag, N. George, H.A. Hamad, IoT-based data-driven predictive maintenance relying on fuzzy system and artificial neural networks, *Sci. Rep.* 13 (2023) 13, <https://doi.org/10.1038/s41598-023-38887-z>.
- [28] F.N. Xu, N. Ding, N. Li, L. Liu, N. Hou, N. Xu, W.M. Guo, L.N. Tian, H.X. Xu, C.M. L. Wu, X.F. Wu, X.F. Chen, A review of bearing failure Modes, mechanisms and causes, *Eng. Fail. Anal.* 152 (2023) 33, <https://doi.org/10.1016/j.engfailanal.2023.107518>.
- [29] F. Dong, H. Yang, H. Du, M. Zhu, Z. Xi, Y. Wang, T. Du, M. Xu, Triboelectric nanogenerator-embedded intelligent bearing with rolling ball defect diagnosis via signal decomposition and automated machine learning, *Nano Energy* 119 (2024) 109072, <https://doi.org/10.1016/j.nanoen.2023.109072>.
- [30] D.K. Dwivedi, *Surface Damage: Causes and Mechanisms*, in: D.K. Dwivedi (Ed.), *Surface Engineering: Enhancing Life of Tribological Components*, Springer India, New Delhi, 2018, pp. 17–43.
- [31] G. Zhu, Y.S. Zhou, P. Bai, X.S. Meng, Q.S. Jing, J. Chen, Z.L. Wang, A shape-adaptive thin-film-based approach for 50% high-efficiency energy generation through micro-grating sliding electrification, *Adv. Mater.* 26 (2014) 3788–3796, <https://doi.org/10.1002/adma.201400021>.
- [32] H.Y. Zou, Y. Zhang, L.T. Guo, P.H. Wang, X. He, G.Z. Dai, H.W. Zheng, C.Y. Chen, A.C. Wang, C. Xu, Z.L. Wang, Quantifying the triboelectric series, *Nat. Commun.* 10 (2019) 9, <https://doi.org/10.1038/s41467-019-09461-x>.
- [33] Y.N. Xie, S.H. Wang, S.M. Niu, L. Lin, Q.S. Jing, J. Yang, Z.Y. Wu, Z.L. Wang, Grating-structured freestanding triboelectric-layer nanogenerator for harvesting mechanical energy at 85% total conversion efficiency, *Adv. Mater.* 26 (2014) 6599–6607, <https://doi.org/10.1002/adma.201402428>.
- [34] Z.L. Wang, On Maxwell's displacement current for energy and sensors: the origin of nanogenerators, *Mater. Today* 20 (2017) 74–82, <https://doi.org/10.1016/j.mattod.2016.12.001>.
- [35] G. Zhu, J. Chen, T.J. Zhang, Q.S. Jing, Z.L. Wang, Radial-arrayed rotary electrification for high performance triboelectric generator, *Nat. Commun.* 5 (2014) 9, <https://doi.org/10.1038/ncomms4426>.
- [36] C.B. Han, C. Zhang, W. Tang, X.H. Li, Z.L. Wang, High power triboelectric nanogenerator based on printed circuit board (PCB) technology, *Nano Res.* 8 (2015) 722–730, <https://doi.org/10.1007/s12274-014-0555-3>.
- [37] L.L. Zu, J. Wen, S.B. Wang, M. Zhang, W.L. Sun, B.D. Chen, Z.L. Wang, Multiangle, self-powered sensor array for monitoring head impacts, *Sci. Adv.* 9 (2023) 11, <https://doi.org/10.1126/sciadv.adg5152>.
- [38] Y. LeCun, Y. Bengio, G. Hinton, Deep learning, *Nature* 521 (2015) 436–444, <https://doi.org/10.1038/nature14539>.
- [39] Q.F. Shi, Z.X. Zhang, T.Y.Y. He, Z.D. Sun, B.J. Wang, Y.Q. Feng, X.C. Shan, B. Salam, C. Lee, Deep learning enabled smart mats as a scalable floor monitoring system, *Nat. Commun.* 11 (2020) 11, <https://doi.org/10.1038/s41467-020-18471-z>.
- [40] Z.X. Zhang, T.Y.Y. He, M.L. Zhu, Z.D. Sun, Q.F. Shi, J.X. Zhu, B.W. Dong, M. R. Yuce, C.K. Lee, Deep learning-enabled triboelectric smart socks for IoT-based gait analysis and VR applications, *npj Flex. Electron.* 4 (2020) 12, <https://doi.org/10.1038/s41528-020-00092-7>.
- [41] A.P. Wibawa, A.B.P. Utama, H. Elmunsyah, U. Pujianto, F.A. Dwiyanto, L. Hernandez, Time-series analysis with smoothed convolutional neural network, *J. Big Data* 9 (2022) 18, <https://doi.org/10.1186/s40537-022-00599-y>.
- [42] A.C. Belkina, C.O. Ciccolella, R. Anno, R. Halpert, J. Spidlen, J.E. Snyder-Cappione, Automated optimized parameters for T-distributed stochastic neighbor embedding improve visualization and analysis of large datasets, *Nat. Commun.* 10 (2019) 12, <https://doi.org/10.1038/s41467-019-13055-y>.
- [43] L. Lin, S.H. Wang, Y.N. Xie, Q.S. Jing, S.M. Niu, Y.F. Hu, Z.L. Wang, Segmentally structured disk triboelectric nanogenerator for harvesting rotational mechanical energy, *Nano Lett.* 13 (2013) 2916–2923, <https://doi.org/10.1021/nl4013002>.
- [44] R.B. Cleveland, W.S. Cleveland, J.E. McRae, I. Terpenning, STL: a seasonal-trend decomposition procedure based on loess, *J. Off. Stat.* 6 (1990) 3–73, in: (<https://www.proquest.com/scholarly-journals/stl-seasonal-trend-decomposition-procedure-based/docview/126680598/se-2>).
- [45] Y.N. Wang, H.Y. Bian, N.H. Yu, Neural network with saliency based feature selection ability, in: 24th IEEE International Conference on Image Processing (ICIP), Ieee, Beijing, PEOPLES R CHINA, 2017, pp. 4502–4506. (<http://doi.org/10.1109/1CIP.2017.8297134>).
- [46] P.J. Tavner, Review of condition monitoring of rotating electrical machines, *IET Electr. Power Appl.* 2 (2008) 215–247, <https://doi.org/10.1049/iet-epa:20070280>.



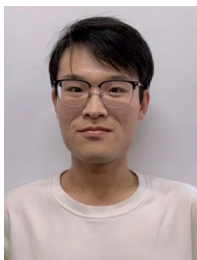
Fangyang Dong received his B.Eng. degree from Dalian Maritime University in 2019, where he is currently pursuing his Ph.D. degree under supervision of Prof. Minyi Xu since 2020. His research focuses on: (1) algorithm development and applications for machine learning and (2) hardware optimization for sensors and robots



Meixian Zhu received his M.S. from Dalian Maritime University in 2024. Currently, he is working for Leapmotor.



Yulian Wang received her B.S. in 2022. Currently, she is as a postgraduate student in Marine Engineering College, Dalian Maritime University. Her current research work focus on artificial intelligence algorithms.



Zhixiang Chen received his B.S. in 2022. Currently, he is as a postgraduate student in Marine Engineering College, Dalian Maritime University. His current research work focus on triboelectric nanogenerators.



Taili Du has been with Dalian Maritime University where he is currently an Associate Professor since 2010. He received his M.S. and PhD. from Dalian Maritime University in China in 2010 and 2023. His current research work focuses on vibration energy harvesting, self-powered sensing and AI-enabled fault diagnosis based on Triboelectric Nanogenerator.



Yingwei Dai received her B.S. in 2022. Currently, she is as a postgraduate student in Marine Engineering College, Dalian Maritime University. Her current research work focus on artificial intelligence algorithms.



Minyi Xu received his Ph.D. degree from Peking University in 2012. During 2016–2017, he joined Professor Zhong Lin Wang's group at Georgia Institute of Technology. Now he is a Professor in the Marine Engineering College, Dalian Maritime University. His current research is mainly focused on the areas of blue energy, self-powered systems, triboelectric nanogenerators and its practical applications in smart ship and ocean.



Ziyue Xi received his B.S. in 2021. Currently, he is as a postgraduate student in Marine Engineering College, Dalian Maritime University. His current research work focus on triboelectric nanogenerators and vibration sensors.